



HAL
open science

Structure Dynamics of Carbon-Supported Platinum-Neodymium Nanoalloys during the Oxygen Reduction Reaction

Carlos Campos-Roldán, Raphaël Chattot, Jean-Sébastien Filhol, Hazar Guesmi, Frédéric Pailloux, Rémi Bacabe, Pierre-Yves Blanchard, Andrea Zitolo, Jakub Drnec, Deborah Jones, et al.

► To cite this version:

Carlos Campos-Roldán, Raphaël Chattot, Jean-Sébastien Filhol, Hazar Guesmi, Frédéric Pailloux, et al.. Structure Dynamics of Carbon-Supported Platinum-Neodymium Nanoalloys during the Oxygen Reduction Reaction. *ACS Catalysis*, 2023, 13 (11), pp.7417-7427. 10.1021/acscatal.3c00371 . hal-04156475

HAL Id: hal-04156475

<https://hal.science/hal-04156475v1>

Submitted on 8 Jul 2023

HAL is a multi-disciplinary open access archive for the deposit and dissemination of scientific research documents, whether they are published or not. The documents may come from teaching and research institutions in France or abroad, or from public or private research centers.

L'archive ouverte pluridisciplinaire **HAL**, est destinée au dépôt et à la diffusion de documents scientifiques de niveau recherche, publiés ou non, émanant des établissements d'enseignement et de recherche français ou étrangers, des laboratoires publics ou privés.

1 Structure Dynamics of Carbon-Supported Platinum-
2 Neodymium Nanoalloys during the Oxygen
3 Reduction Reaction

4 *Carlos A. Campos-Roldán†, Raphaël Chattot†, Jean-Sébastien Filhol,† Hazar Guesmi,†*
5 *Frédéric Pailloux‡, Rémi Bacabe,† Pierre-Yves Blanchard†, Andrea Zitolo,¶ Jakub Drnec,¶*
6 *Deborah J. Jones†, Sara Cavaliere †**

7
8 † ICGM, Univ. Montpellier, CNRS, ENSCM, 34095 Montpellier cedex 5, France

9 ‡ Institut P², CNRS - Université de Poitiers – ISAE-ENSMA - UPR 3346, 11 Boulevard Marie et
10 Pierre Curie, Site du Futuroscope, TSA 41123, 86073 Poitiers cédex 9, France

11 ¶ Synchrotron SOLEIL, L'Orme des Merisiers, BP 48 Saint Aubin, 91192 Gif-sur-Yvette,
12 France

13 ¶ ESRF, European Synchrotron Radiation Facility, 71 Avenue des Martyrs, CS40220, 38043
14 Grenoble Cedex 9, France

15
16 *Corresponding author: sara.cavaliere@umontpellier.fr
17

18
19
20
21 **KEYWORDS:** Pt alloys, Rare Earth Metals, Operando measurements, Oxygen Reduction
22 Reaction, Proton Exchange Membrane Fuel cells.

23 **ABSTRACT**

24 Platinum-rare earth nanoalloys have been predicted to be promising proton exchange membrane
25 fuel cell (PEMFC) electrocatalysts for the cathodic oxygen reduction reaction (ORR). However,
26 their implementation in PEMFCs is limited by the challenge of their preparation as carbon-
27 supported nanostructures. Consequently, the practical structure-activity-stability trends for this
28 class of nanoalloys remain largely unexplored. Herein, carbon-supported Pt-Nd nanoalloys as
29 ORR electrocatalysts are described. The physical chemistry of selected electrocatalysts was
30 extensively investigated by means of combined *ex situ* and *operando* techniques, which reveal the
31 unique structural dynamics of Pt-Nd nanoalloys in a simulated PEMFC cathode environment. The
32 experimental observations, supported by theoretical calculations, indicate that after initial
33 significant structural modification in the early stage of operation, the ORR activity is mediated in
34 the longer-term by surface compressive strain rather than charge transfer between Pt and Nd. Such
35 key *operando* structure-activity-stability relations underpin further optimization of carbon-
36 supported Pt-rare earth nanoalloys as fuel cell cathode catalysts.

37

38 **1. INTRODUCTION**

39 Proton-exchange membrane fuel cells (PEMFCs) are considered as suitable devices to contribute
40 to the CO₂ neutrality targets,¹ and have gained much attention for use in heavy-duty and long-
41 distance transportation due to the high gravimetric energy density of hydrogen.² Notwithstanding,
42 the massive implementation of PEMFCs is still hindered by technical barriers that need to be
43 overcome, including performance, durability, cost and fuel efficiency.^{3,4} In fact, the performance
44 of a PEMFC has an important dependency on the catalyst layers,⁵ which usually possess high Pt

45 loadings specially at the cathode, where the sluggish oxygen reduction reaction (ORR) takes place.
46 Therefore, tailoring high-performance Pt-based electrocatalysts for the ORR is of paramount
47 importance, which current target is to use 0.1 g_{PGM}/kW (platinum-group metal, PGM) for
48 automotive and 0.3 g_{PGM}/kW for heavy-duty transport applications.²

49
50 A widely used strategy to increase the activity of ORR electrocatalysts is by alloying Pt with late
51 transition metals (usually Ni, Co, Fe, Cu, *etc*), which also decreases simultaneously the amount of
52 Pt.⁵ However, the long-term stability of these materials represents a crucial issue that must be
53 overcome.^{6, 7} In this context, Pt-rare earth metal (Pt-REM) alloys have been proposed as a
54 promising family of highly active/stable electrocatalysts for the ORR.⁸ Theoretical studies
55 suggested that the exceptionally negative formation energy of Pt-REM alloys represents a kinetic
56 barrier to diffusion of the REM atom, and impedes the alloy degradation.^{8,9} Experimental evidence
57 with bulk sputter-cleaned polycrystalline electrodes¹⁰⁻¹³ and unsupported nanoparticles (NPs)^{14, 15}
58 revealed that the high activity of these alloys (including the cubic structure Pt₃Y system) stems
59 from the formation of a specific structure, in which the Pt-REM alloy is protected by a Pt-rich
60 overlayer,¹⁶ which experiences a lateral compressive strain.^{11, 16} Indeed, the surface specific ORR
61 activity showed an exponential dependence on the degree of compressive strain in the Pt-REM
62 alloys.^{14, 15}

63
64 Escudero-Escribano *et al.*¹³ correlated the ORR specific activity of Pt₅REM sputter-cleaned
65 polycrystalline electrodes (REM = La, Ce, Sm, Gd, Tb, Dy, Tm) to the *ex situ* measured Pt lattice
66 parameter. Pt₅REM forms a hexagonal crystalline structure, the atomic arrangement of which

67 stabilizes the so-called *kagome* layer.¹⁶ This particular configuration presents an unusual CaCu₅-
68 like structure that accommodates the alloying elements of different atomic radius in a different
69 way from face centered cubic (FCC) or hexagonal close packed (HCP) alloys, to form uniform
70 bond lengths between Pt-Pt, Pt-REM and REM-REM:¹⁶ the CaCu₅ structure consists of alternating
71 layers of Pt₂REM and Pt₃ layers. The pure Pt layers in bulk Pt₅M alloys have hollow vacancy-like
72 spaces at positions below and above the REM atoms. This results in a compressed Pt overlayer
73 despite alloying Pt with larger REM atoms, which can be explained by the hexagonal symmetry
74 of both the Pt(111) surface and the Pt₅REM bulk structure. In fact, the lattice parameter *a* in the
75 hexagonal structure continues its contraction while moving towards the so-called lanthanide
76 contraction, but the *b* and *c* lattice parameters are considerably different due to the different re-
77 organization of the atoms. Namely, for Pt-REM alloys with the CaCu₅-like structure, the unit cell
78 *a* will contract (shorter Pt-Pt distances) as the REM covalent radii decreases (lanthanide
79 contraction).¹³ *Ex situ* measurements of the imposed compressive strain in the Pt lattice revealed
80 that the specific ORR activity is highest at a contraction of -3 %, respect to Pt bulk.¹³

81

82 Nevertheless, the limited availability of carbon-supported Pt-REM nanostructures has restricted
83 the transposition of the results obtained on model extended surfaces to practical PEMFCs. Indeed,
84 synthesis of nanoparticle Pt-REM alloys is challenging due to the highly negative standard redox
85 potential of rare earth metals (far beyond the stability range of water) and their high oxophilicity,
86 which favours formation of REM oxygen-containing species instead of alloys.¹⁷ Although recent
87 synthesis approaches¹⁷⁻²⁰ have enabled the preparation of carbon-supported Pt-REM nanoalloys,
88 their reported ORR mass activity (between 0.3 - 0.7 A mg_{Pt}⁻¹)²¹⁻²³ is far below that of unsupported

89 9 nm Pt_xY¹⁴ NPs (3.05 A mg_{Pt}⁻¹) or 8 nm Pt_xGd¹⁵ NPs (3.60 A mg_{Pt}⁻¹). Therefore, further
90 understanding and optimization of Pt-REM/C nanoalloys are still needed.

91
92 *In situ* and/or *operando* techniques, such as X-ray diffraction (XRD), X-ray absorption
93 spectroscopy (XAS), *online* inductively coupled plasma mass spectrometry (ICP-MS), *etc.*, are
94 essential tools to understand electrocatalyst behaviour in real or simulated electrochemical
95 environments of the application device. Indeed, it is largely accepted that fundamental reactivity
96 descriptors (*e.g.* surface strain, chemistry and/or crystallinity) of Pt-based electrocatalysts
97 measured and tailored *ex situ* are not necessarily conserved *in situ*²⁴⁻²⁷ due to surface reconstruction
98 in the particular environment of the PEMFC cathode on operation.^{24, 28} Indeed, to the best of our
99 knowledge, such *In situ* and/or *operando* techniques has never been used to investigate this
100 promising novel class of Pt-REM/C nanoalloys.

101
102 In this contribution, we describe the synthesis and extensive characterization of carbon-supported
103 Pt-Nd nanoalloys. By adjusting the quantity of the Nd chemical precursor during the synthesis, the
104 Pt:Nd composition in the final electrocatalyst was systematically modulated and the ORR activity
105 was tailored. Two Pt-Nd/C electrocatalysts of different crystal structure were selected on the basis
106 of their high ORR activity, and were investigated by means of an extensive range of combined *ex*
107 *situ* (WAXS, XAS, HRTEM, STEM/EELS, ICP-MS) and *operando* (WAXS) techniques. The *ex*
108 *situ* and *operando* structural properties of the selected materials were rationalized and compared,
109 to shed new light on the *operando* structure-activity-stability relationships of carbon-supported Pt-
110 REM nanoalloys.

111

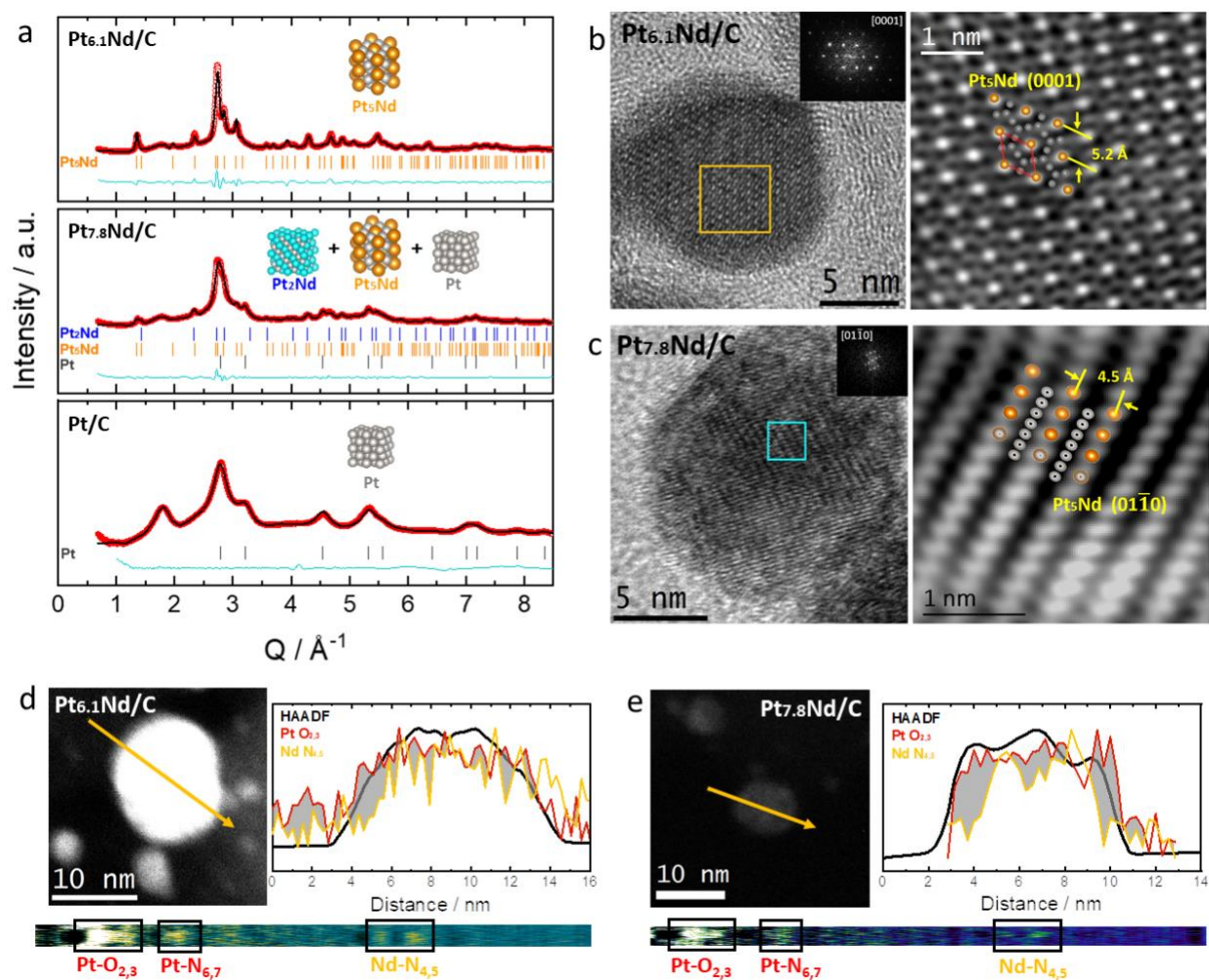
112 3. RESULTS AND DISCUSSION

113 We have prepared Pt-Nd/C nanoalloys using the carbodiimide complex route proposed by Hu *et*
114 *al.*¹⁸ with some modifications^{29, 30} (see Supplementary Information S1). Firstly, five Pt:Nd atomic
115 ratios (16.5:1, 7.8:1, 6.1:1, 5.7:1 and 5.4:1) were obtained by systematically varying the Nd
116 precursor content in the synthesis. The Pt_xNd/C catalyst series prepared was subsequently
117 characterized by means of XRD, ICP-MS and electron microscopy, and their electrocatalytic
118 activity was investigated using the RDE technique in 0.1 M HClO₄ electrolyte (see Supplementary
119 Information S6). This preliminary screening revealed that the Pt_{7.8}Nd/C and Pt_{6.1}Nd/C
120 electrocatalysts present the highest activity for the ORR among the series (0.55 A mg_{Pt}⁻¹ and 0.63
121 A mg_{Pt}⁻¹ at 0.9 V_{RHE}, respectively), surpassing the reference Pt/C material from Johnson-Matthey
122 (0.24 A mg_{Pt}⁻¹). Interestingly, and despite relatively close overall chemical composition and ORR
123 activity, the crystalline structures of these two materials revealed by XRD are different, with
124 Pt_{6.1}Nd/C presenting only the Pt₅Nd hexagonal phase and Pt_{7.8}Nd/C a mixture of cubic Pt, cubic
125 Pt₂Nd and hexagonal Pt₅Nd phases. These two electrocatalysts were selected as model samples for
126 a more comprehensive understanding of the structure-activity-stability trends in this class of
127 nanoalloys.

128 Rietveld full profile refinement of the wide-angle synchrotron X-ray scattering (WAXS) patterns
129 of Pt_{7.8}Nd/C and Pt_{6.1}Nd/C collected *ex situ*, see Figure 1a, confirms the above results obtained
130 from laboratory-source XRD. Quantitative phase analysis indicates that the Pt_{7.8}Nd/C sample
131 comprises 51 wt.% hexagonal Pt₅Nd, 37 wt.% FCC Pt and 12 wt.% cubic Pt₂Nd crystalline phases,
132 and that the Pt_{6.1}Nd/C sample is 100 wt.% hexagonal Pt₅Nd crystal structure. Further

133 microstructural parameters, such as the lattice constants of these phases and their associated
 134 coherent domain sizes, were extracted from the Rietveld refinement, and are shown in Table 1.
 135 Compared to the reference Pt/C electrocatalyst, the nearest neighbour Pt-Pt distances are shorter
 136 in the Pt₂Nd and Pt₅Nd crystalline arrangements, corresponding to a compressive strain of *ca.* -2%
 137 and -3%, respectively.

138



139
 140 **Figure 1.** (a) Refined *ex situ* WAXS patterns (vertical bars represent the theoretical diffraction
 141 pattern of each crystalline phase, and the cyan line represents the residual from the refinement);
 142 representative HRTEM micrographs of (b) Pt_{6.1}Nd/C and (c) Pt_{7.8}Nd/C; and (c) representative
 143 HAADF-STEM/EELS analysis of (d) Pt_{6.1}Nd/C and (e) Pt_{7.8}Nd/C. Pt/C is used as reference in (a).

144 **Table 1.** Chemical composition, particle size and refined structural data of Pt_{6.1}Nd/C and
 145 Pt_{7.8}Nd/C. Pt/C is used as reference.

	^a Metal content (%wt.)	^a Pt:Nd ratio	^b Mean particle size (nm)	Crystalline phase weight fraction (%)	Lattice parameter a (Å)	^c Lattice parameter c (Å)	Coherent domain size (nm)	Pt – Pt distance (Å)	^d ε (%)
Pt _{7.8} Nd/C	Pt: 26.67 Nd: 2.52	7.8 : 1	6.1 ± 1.6 *12.8 ± 1.7	Pt ₅ Nd: 51 Pt ₂ Nd: 12 Pt: 37	Pt ₅ Nd: 5.357 Pt ₂ Nd: 7.644 Pt: 3.914	Pt ₅ Nd: 4.421	Pt ₅ Nd: 4.0 Pt ₂ Nd: 5.3 Pt: 3.2	Pt ₅ Nd: 2.678 Pt ₂ Nd: 2.702 Pt: 2.767	Pt ₅ Nd: -3.1 Pt ₂ Nd: -2.2 Pt: 0.1
Pt _{6.1} Nd/C	Pt: 27.04 Nd: 3.29	6.1 : 1	6.8 ± 1.5 *13.1 ± 2.1	Pt ₅ Nd: 100	Pt ₅ Nd: 5.364	Pt ₅ Nd: 4.408	Pt ₅ Nd: 9.5	Pt ₅ Nd: 2.682	Pt ₅ Nd: -3.0
Pt/C	Pt: 47.2	--	3.7 ± 0.9	Pt: 100	Pt: 3.909	--	Pt: 1.6	Pt: 2.764	0

146 a: Determined by ICP-MS; b: Determined by TEM; c: in a hexagonal structure a=b≠c; d: Relative
 147 to Pt/C. * Average size of agglomerates.

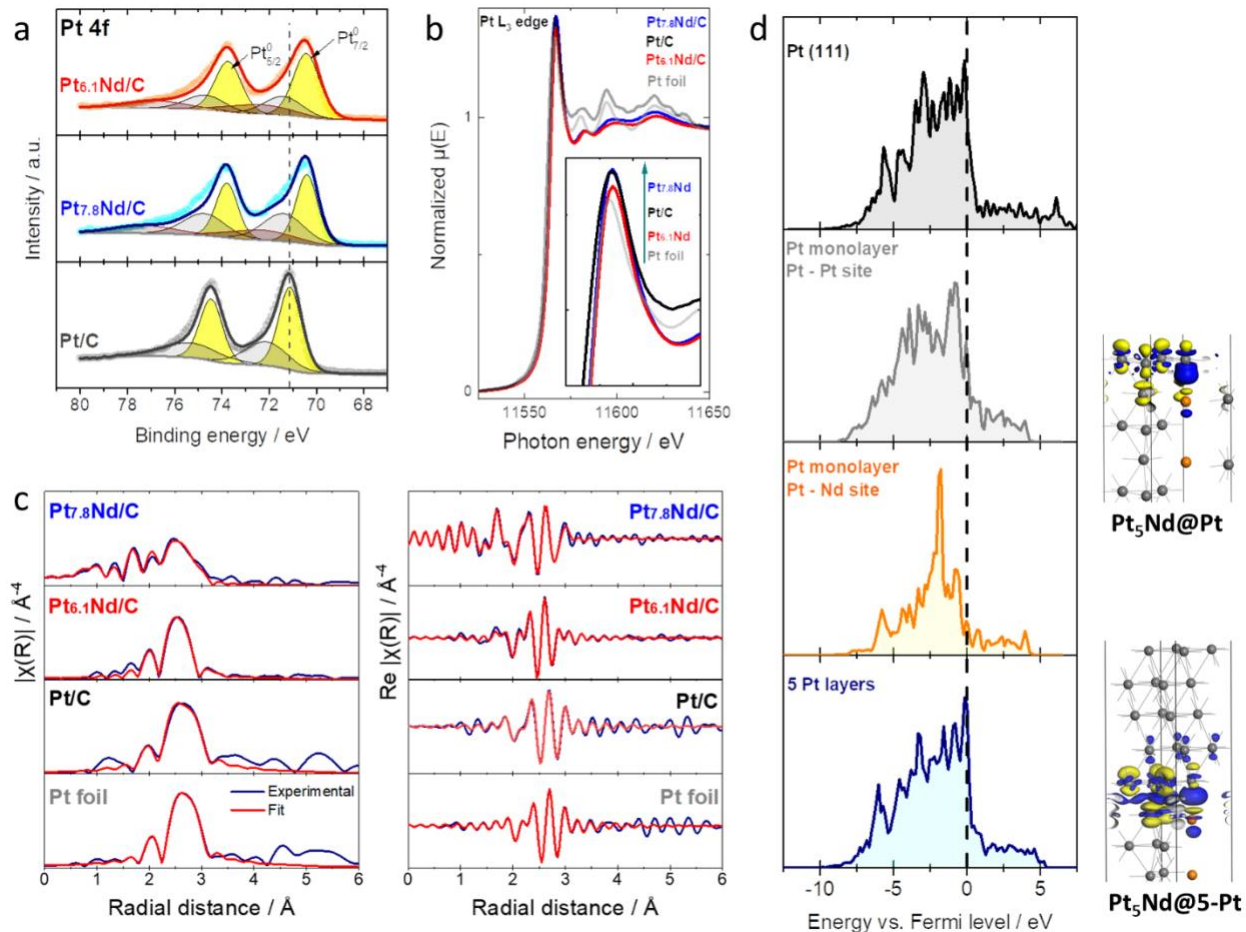
148

149 High resolution TEM overviews and the corresponding power spectrum on isolated NPs, Figure
 150 1b and c, resolve the atomic arrangements in both materials, where the Pt₅Nd (0001) and the Pt₅Nd
 151 (01 $\bar{1}$ 0) crystalline planes are observed for Pt_{6.1}Nd/C and Pt_{7.8}Nd/C, respectively. For both
 152 electrocatalysts, the results of combined HAADF-STEM and EELS analyses, Figure 1d and 1e,
 153 also confirm the presence of both Pt and Nd in the NPs. Due to the difference between the Pt and
 154 Nd dissolution potentials and the post-synthesis acidic wash (4 h in N₂-saturated 0.5 M H₂SO₄), it
 155 is expected the stabilization of a Pt-rich shell surrounded the alloy structure.³¹ Based on the
 156 computed phase diagram of the possible structures and their associated stabilities (see the
 157 Supplementary Information S9), a pure Pt monolayer over the Pt₅Nd alloy (Pt₅Nd@Pt) is a quite
 158 stable structure. Considering that the thickness of an atomic monolayer of Pt is ~ 0.2 nm, and that
 159 the probe size and the probe step in the HAADF-STEM/EELS were 0.5 nm and 0.4 nm
 160 respectively, the detection of one atomic Pt monolayer is clearly below the detection limit of the

161 microscope used. Therefore, the presence of Pt₅Nd@Pt with a thinner Pt overlayer or structures
162 with Pt-rich multilayers cannot be ruled out.

163 The near-surface composition was investigated by XPS. Figure 2a shows the Pt 4*f* photoemission
164 lines, which indicates the predominance of the Pt metallic state at the near-surface region in all
165 cases (the survey spectra and the Nd 3*d* photoemission lines are given in the Supplementary
166 Information S7). However, the binding energy position of the Pt metallic doublet in Pt_{7.8}Nd/C and
167 Pt_{6.1}Nd/C is downshifted with respect to that of the Pt/C reference, suggesting a modification of
168 the Pt electronic structure. The alloy formation energy ($\Delta H^{\circ}_{\text{Pt5Nd}} = -55 \text{ kJ g}^{-1} \text{ atom}^{-1}$)³² correlates
169 with the difference in electronegativity between the alloying metals,³³ leading to charge transfer
170 from Nd ($\chi_{\text{Nd}} = 1.14$) to Pt ($\chi_{\text{Pt}} = 2.28$) and increased electron density around Pt. Besides,
171 compressive strain, *i.e.*, shorter Pt-Pt interatomic distances, might also modify the electronic states
172 of Pt due to the overlapping of the electron conduction bands.³⁴

173



174

175 **Figure 2.** (a) Pt 4f photoemission lines (Pt/C is used as reference); *ex situ* Pt L₃ edge (b) XANES
 176 and (c) fitted FT EXAFS spectra (Pt foil and Pt/C are used as reference) of Pt_{6.1}Nd/C and Pt_{7.8}Nd/C.
 177 (d) Projected density of states (PDOS) of Pt surface atoms from Pt (111) surface, Pt₅Nd@Pt or
 178 Pt₅Nd@5-Pt. To show the effect of sub-surface Nd on the electronic structure of surface Pt in
 179 Pt₅Nd@Pt, the PDOS on different surface Pt atom either on top of a subsurface Nd atom or above
 180 3 subsurface Pt atoms are represented.

181

182 The local electronic structure and coordination environment of Pt in the electrocatalysts was
 183 studied using X-ray absorption spectroscopy (XAS). The *ex situ* X-ray absorption near-edge
 184 structure (XANES) at the Pt L₃ edge are shown in Figure 2b for Pt_{7.8}Nd/C and Pt_{6.1}Nd/C. As
 185 reference, Pt/C and the Pt foil were used. The white line intensity in the XANES spectra indicates

186 the transition from occupied Pt $2p$ electrons to empty Pt $5d$ states. Therefore, this parameter is
187 indicative of the Pt $5d$ band occupancy,²⁴ with a higher white line intensity suggesting higher
188 density of unoccupied valence states at Pt sites (more vacancies) respect to the Pt foil. As seen in
189 Figure 2b, the white line intensity follows the trend Pt foil < Pt_{6.1}Nd/C < Pt/C ≤ Pt_{7.8}Nd/C. The
190 average first-shell Pt-Pt bond lengths were determined by fitting the filtered Fourier Transform X-
191 ray absorption fine structure (EXAFS) spectra, shown in Figure 2c and Supplementary Information
192 S8 respectively. The nearest neighbor Pt-Pt interatomic distances are shorter for Pt_{6.1}Nd/C and
193 Pt_{7.8}Nd/C than in the reference Pt/C and Pt foil, which reflects a compressive strain of *ca.* -3 %
194 and -1.6 % respectively, in agreement with the refined WAXS parameters.

195

196 Density functional theory (DFT) calculations were carried out to gain more information on the
197 electronic structure of the Pt-Nd electrocatalysts. As was mentioned above, the optimization of
198 several alloyed Pt₅Nd systems, through the calculation of their grand potential as a function of the
199 Pt chemical potential (see details in the Supplementary Information S9), predicts the stability of a
200 slab with a pure Pt monolayer (Pt₅Nd@Pt) and the metastability of thicker Pt-covered slabs with
201 5 Pt overlayers (Pt₅Nd@5-Pt), which agrees with the experimental data shown in Figure 1. Such
202 structures are compressively strained relative to the Pt (111) reference, with shorter Pt-Pt
203 interatomic distances in the x - y plane, of average value of 2.67 Å (2.75 Å for the Pt reference), in
204 line with the experimental results.

205

206 Interestingly, in the Pt₅Nd@Pt structure model, the Pt atom of the monolayer just above the Nd
207 atom appears to be electron-enriched, while Nd undergoes an electron loss (Figure 2d), suggesting

208 a strongly polarized bond between $\text{Pt}^{\delta-}$ and $\text{Nd}^{\delta+}$. In fact, the surface work function of $\text{Pt}_5\text{Nd@Pt}$
209 (5.53 eV) is computed to be lower than that of Pt (111) (5.70 eV), which confirms electronic
210 enrichment of the surface. This increased electron density on Pt might be reflected in the downshift
211 observed by XPS in the Pt 4f region (Figure 2a). The computed projected densities of states
212 (PDOS), *c.f.* Figure 2d, exhibits a strong narrow peak for the Pt located on top of the subsurface
213 Nd (associated with the Pt- d_{z^2} orbital), which suggests a decrease of its orbital overlaps with the
214 surrounding atoms, in agreement with the formation of a Pt-Nd partially ionic bond. Thus, this Pt
215 site on $\text{Pt}_5\text{Nd@Pt}$ has a specific reactivity between a delocalized surface and an isolated atomic
216 structure.

217

218 In the case of the $\text{Pt}_5\text{Nd@5-Pt}$ structure, although the Pt atoms at the interface with Pt_5Nd create
219 similar bonding associated with a charge transfer from Nd toward the closest Pt atoms as for the
220 case of $\text{Pt}_5\text{Nd@Pt}$, no significant charge transfer from Nd is found to occur beyond the two first
221 neighboring Pt layers. However, the Pt atoms at the surface still experience compressive strain,
222 induced by the epitaxy on the Pt_5Nd alloy. Thus, the modification of the surface electronic
223 properties is due to an increase of the d -band width compared to Pt (111), which results from the
224 stronger d -orbital overlapping,³⁵ as is confirmed by the corresponding PDOS shown in Figure 2d.
225 In both cases, the electronic modifications close to the Fermi level will induce changes in the
226 surface reactivity, and modulate the adsorption energies of adsorbates.^{36, 37}

227

228 At this point and based on the *ex situ* characterization of $\text{Pt}_{6.1}\text{Nd/C}$ and $\text{Pt}_{7.8}\text{Nd/C}$, it might be
229 expected that both electrocatalysts are particular active for the ORR. However, the observed

230 activity enhancement, in terms of mass activity, is only *ca.* 3-fold respect to the Pt/C benchmark.
231 *Operando* WAXS measurements were carried out to follow any modification of the electrocatalyst
232 structure during the electrochemical operating conditions. Conventional thin-film electrodes (20
233 $\mu\text{g}_{\text{Pt}} \text{cm}^{-2}_{\text{geo}}$) on glassy carbon substrates were mounted in a dedicated X-ray-transparent
234 electrochemical flow cell described in a previous contribution²⁶ filled with N₂-saturated 0.1 M
235 HClO₄ electrolyte and kept at the open circuit potential (OCP) prior to any measurement (see
236 Supplementary Information S4 for more details). The electrochemical test protocol started with
237 electrode preconditioning (or electrochemical activation) procedure, consisting of potential
238 cycling between 0.05 and 0.95 V_{RHE} at 100 mV s⁻¹ for 20 cycles. WAXS patterns were collected
239 with 1 s temporal resolution. For both Pt_{6.1}Nd/C and Pt_{7.8}Nd/C electrocatalysts, significant
240 structural changes were observed even upon the early electrochemical activation, which are shown
241 in Figures 3 and 4, respectively.

242

243 In the case of Pt_{6.1}Nd/C, Figures 3a-b show that the first cathodic scan (from the OCP to 0.05
244 V_{RHE}) triggers the sudden growth of a pure Pt FCC phase. This crystalline phase (initially absent
245 from the pristine sample) further evolves as soon as the electrode potential passes below 0.32 V_{RHE}
246 (Figure 3b) and reaches a stable weight fraction of *ca.* 20 wt.% after only one second. For
247 Pt_{7.8}Nd/C, Figures 4a-b show that, during the first cathodic scan, the pure Pt FCC phase (already
248 present in the pristine sample) further increases once the electrode potential passes below 0.80
249 V_{RHE} and reaches a stable weight fraction of *ca.* 65 wt.% after *ca.* 10 seconds. The Pt₂Nd cubic
250 phase that was detected in the pristine Pt_{7.8}Nd/C sample was not observed *operando*, but rather an
251 increased fraction of the Pt FCC instead. This suggests the Pt₂Nd phase converted to Pt FCC during
252 the hold of the electrode at OCP (*ca.* 20 min during cell alignment with the X-ray beam),

253 highlighting the low stability of the Pt₂Nd crystalline structure under the electrochemical
254 conditions.

255

256 For both samples, the origin of the Pt atoms constituting the growing Pt FCC phase might be
257 correlated with the evolution of the individual phase intensities or scale factors (Figure 3c and 4c).

258 However, the appearance of the Pt FCC phase is not correlated to the change in the intensity of

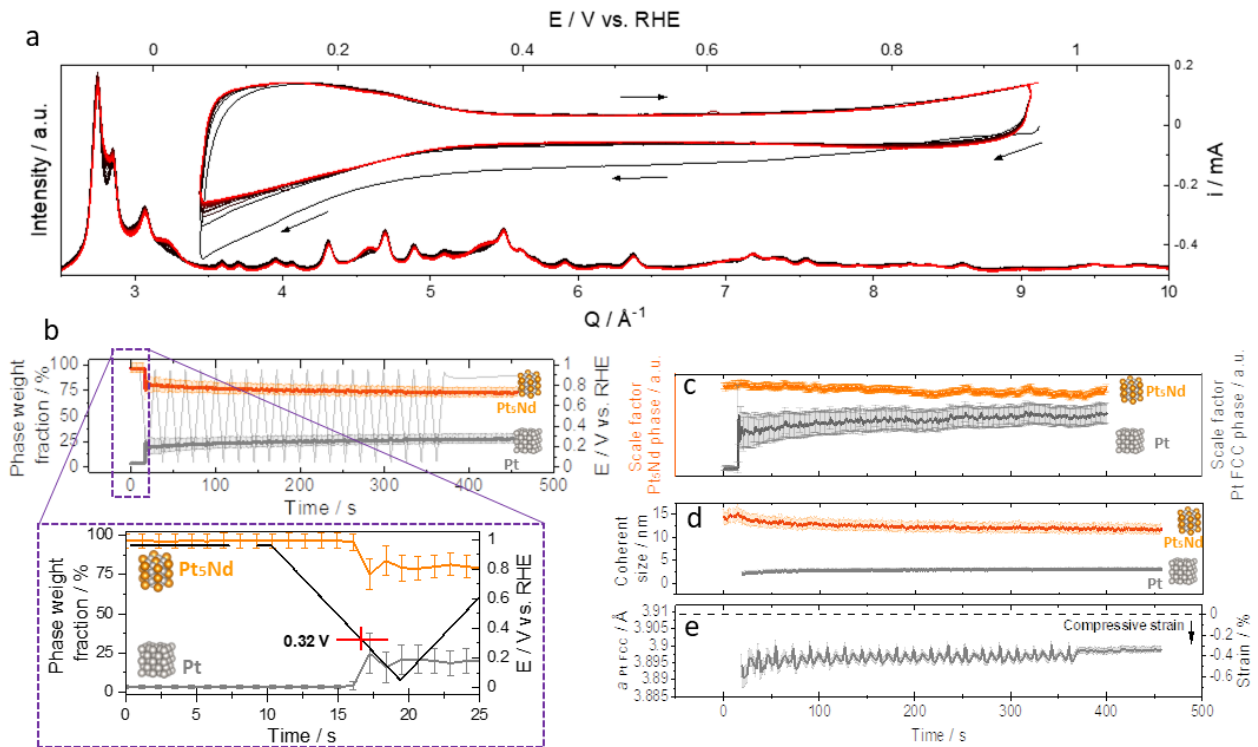
259 Pt₅Nd, which suggests that the origin of the Pt FCC comes from the electrochemical reduction of

260 an amorphous phase containing Pt (*e.g.*, amorphous Pt oxides). The slight decrease of the Pt₅Nd

261 phase intensity during the subsequent electrochemical activation suggests, in both cases, possible

262 phase conversion from the hexagonal Pt₅Nd to Pt FCC, but only to a minor extent.

263

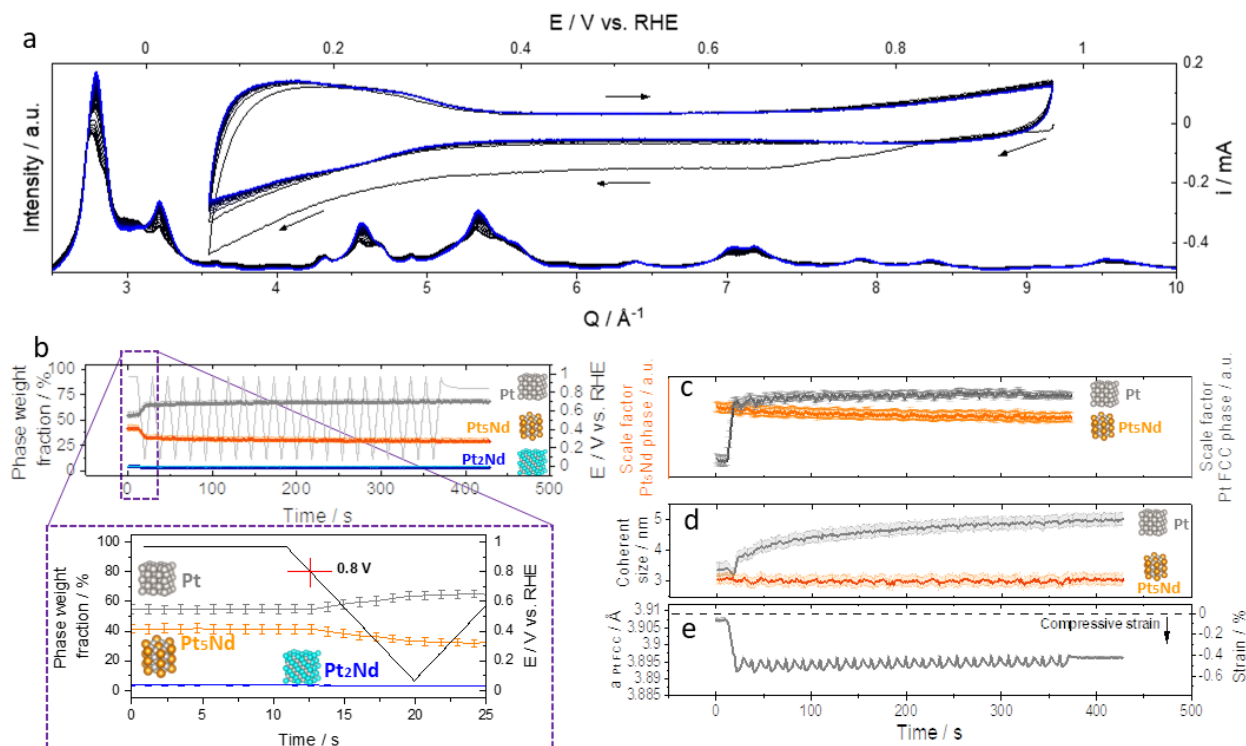


264

265 **Figure 3.** *Operando* WAXS analysis during the electrochemical activation of Pt_{6.1}Nd/C: (a) cyclic
266 voltammogram and *operando* WAXS patterns (the arrows indicate the polarization direction); and
267 refined microstructural parameters extracted from the WAXS patterns: (b) phase weight fractions,
268 (c) scale factors, (d) coherent domain sizes, and (e) lattice parameter and relative strain.

269
270 For Pt_{6.1}Nd/C, further analysis reveals that the average coherent domain size of the Pt₅Nd phase
271 decreases from 15 nm to 10 nm at the end of the electrochemical activation, and that the coherent
272 domain size of the Pt FCC phase increases to *ca.* 3 nm, Figure 3d. This behaviour is consistent
273 both with the partial phase transition from Pt₅Nd to Pt FCC triggering the formation of thicker Pt
274 overlays, and/or small pure Pt NPs are formed. The computed phase diagram (see the
275 Supplementary Information S9) predicts that Pt multilayer deposits on the Pt₅Nd phase could
276 remain kinetically stable as slow Pt diffusion should impair the nucleation of pure Pt NPs.
277 Otherwise, the multilayer deposits could nucleate into pure Pt NPs. For Pt_{7.8}Nd/C, the results of
278 Figure 4d indicate that during the electrochemical activation the average coherent domain size of
279 the Pt₅Nd phase seems almost constant (*ca.* 3 nm), however, the coherent domain size of the Pt
280 FCC phase seems to increase from *ca.* 3 nm to *ca.* 5 nm. This increase in size might also be related
281 to the conversion of Pt₂Nd to Pt FCC.

282



283
 284 **Figure 4.** *Operando* WAXS analysis during the electrochemical activation of Pt_{7.8}Nd/C: (a) cyclic
 285 voltammogram and *operando* WAXS patterns (the arrows indicate the polarization direction); and
 286 refined microstructural parameters extracted from the WAXS patterns: (b) phase weight fractions,
 287 (c) scale factors, (d) coherent domain sizes, and (e) lattice parameter and relative strain.

288
 289 For both electrocatalysts, the refined average lattice parameter of the Pt FCC phase, a_{PtFCC} , is
 290 smaller relative to the reference Pt/C (dashed black line in Figures 3e and 4e), indicating that this
 291 crystalline phase is under compressive strain. The compressive strain in both cases reaches *ca.* -
 292 0.4 % at the end of the electrochemical activation. Notwithstanding, the *operando* average strain
 293 is significantly lower than that measured *ex situ*. The model derived from DFT proposes that as
 294 the Pt shell thickness increases (higher number of Pt layers over the Pt₅Nd structure) the Pt-Pt
 295 interatomic distances through the *z*-axis increase (lattice dilation, see Figure S11 in the
 296 Supplementary Information S9), while the surface Pt atoms experience lateral compressive strain

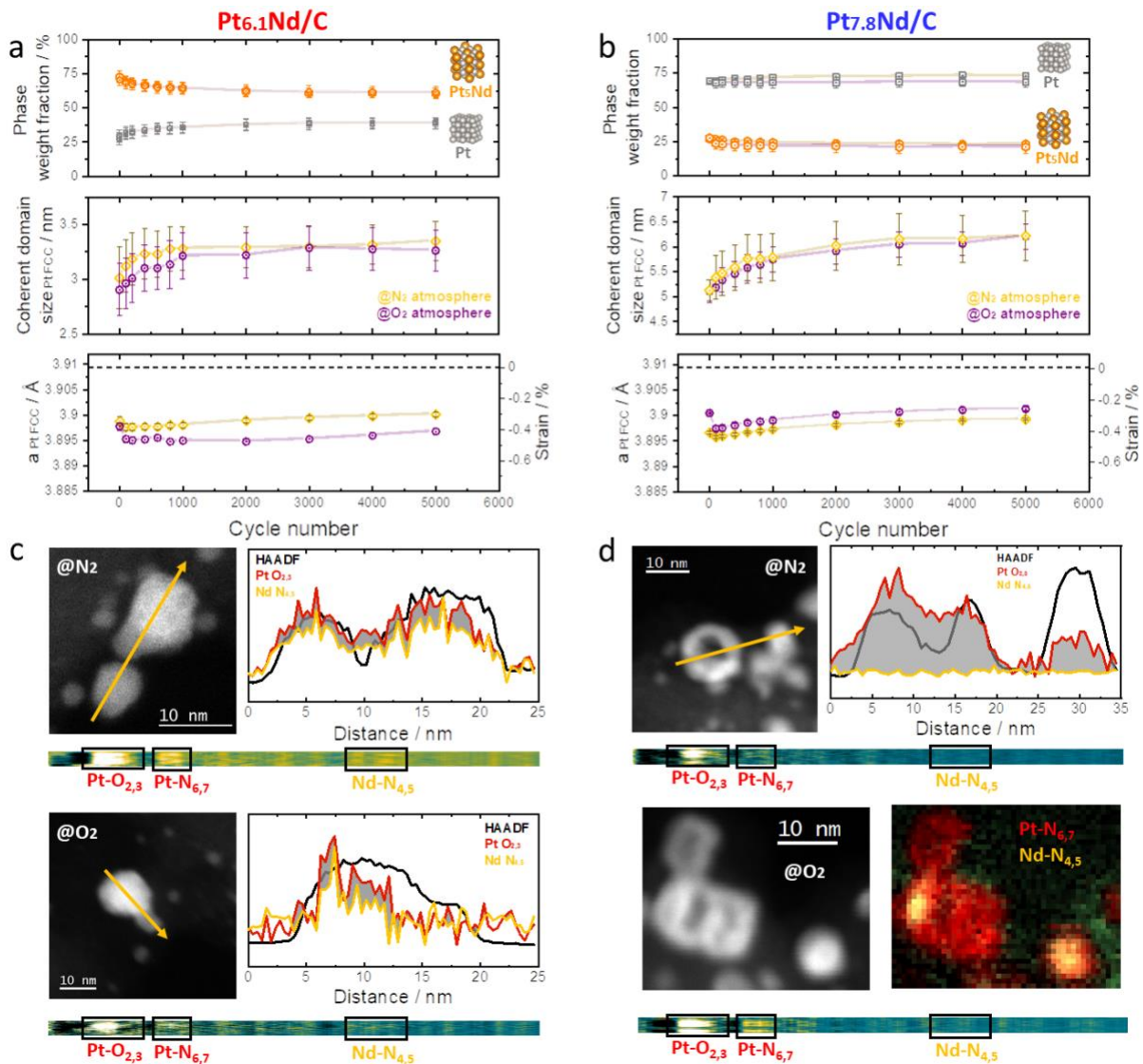
297 along the x - y plane. The average residual strain is approximately -0.89 %, suggesting a
298 counterbalance between compressive and tensile strain.

299

300 The structural evolution of the $\text{Pt}_x\text{Nd}/\text{C}$ electrocatalysts was followed through an accelerated
301 degradation test (ADT), *c.f.* Figure 5, that used 5,000 square-wave potential cycles between 0.6-
302 0.95 V_{RHE} ³⁸ (see the Figure S1 in the Supplementary Information S3). The ADT was carried out
303 under both N_2 - and O_2 - saturated 0.1 M HClO_4 , although no significant structural difference was
304 observed for catalysts aged in these different atmospheres over 5,000 cycles.

305

306 For $\text{Pt}_{6.1}\text{Nd}/\text{C}$, the phase weight fraction of the Pt_5Nd alloy decreases slightly from *ca.* 75 % to 70
307 % after 5,000 cycles, and the FCC Pt phase weight fraction increases from *ca.* 25 % to 30 % after
308 the ADT. The most pronounced phase transitions take place during the first 500 electrochemical
309 cycles, little further modification occurring thereafter. The average coherent domain size of the Pt
310 FCC phase grew during the ADT from *ca.* 3 nm to 3.25 nm. The a_{PtFCC} is shorter respect to the Pt
311 reference during the ADT, pointing out a compressive strain, which is gently relaxed at the end of
312 the ADT. The HAADF-STEM micrographs and the EELS chemical profiles after the ADT, *c.f.*
313 Figure 5c and Supplementary Information S10, indicate the predominance of dense NPs, the
314 chemical composition of which comprises both Pt and Nd. Even though the thickening of the Pt
315 overlayer might be expected, this feature does not fully explain the increase of the average Pt FCC
316 phase weight fraction nor its increased average coherent domain size. If we assume the presence
317 of solid NPs with a Pt-rich overlayer thickness of 1 nm (~ 5 Pt atomic layers, see below), the
318 remaining contribution of the Pt FCC is probably related to the presence of pure Pt NPs.



320

321 **Figure 5.** Refined WAXS parameters (weight fraction, coherent domain size, lattice parameter
 322 and relative strain) of the crystalline phases detected during the applied ADT of (a) Pt_{6.1}Nd/C and
 323 (b) Pt_{7.8}Nd/C. Representative STEM/EELS chemical mapping of (d) Pt_{6.1}Nd/C and (c) Pt_{7.8}Nd/C
 324 after the ADT.

325

326 In contrast, in the case of Pt_{7.8}Nd/C, the Pt FCC phase is clearly predominant (*ca.* 75 %*wt.*) relative
 327 to the Pt₅Nd alloy (*ca.* 25 %*wt.*). This behaviour is constant along the whole ADT. The average

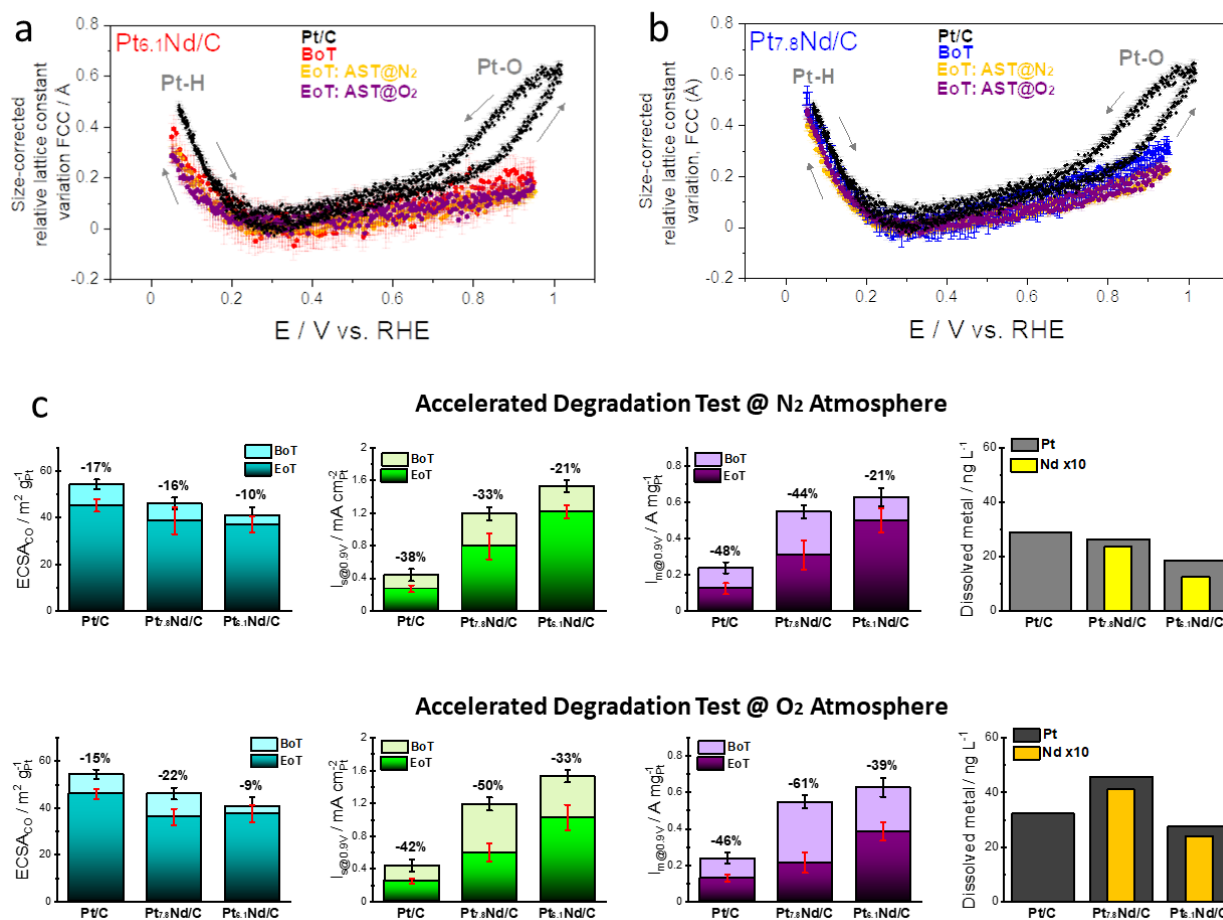
328 coherent domain size of the Pt FCC phase, indeed, increases with the cycle number, indicating the
329 formation of bigger Pt crystalline domains during the ADT, from ~ 5 nm to ~ 6.5 nm. At the end
330 of the ADT, the trend follows an upward behaviour, suggesting the continuous increment of the Pt
331 crystalline domains. Meanwhile, the lattice parameter a_{PtFCC} indicates a trend towards lattice
332 relaxation as the cycle number increases. The STEM micrographs and the EELS chemical profiles
333 after the ADT shown in Figure 5d and Supplementary Information S10 reveal the predominance
334 of hollow Pt structures, these architectures corresponding to the dominant Pt FCC phase. Clearly,
335 the growing coherent domain size trend testifies to the loss of the Pt-Nd alloy, and the stabilization
336 of Pt hollow architectures. Interestingly, the EELS mapping shown in Figure 5d (ADT@O₂)
337 reveals the presence of solid core/shell NPs with a Pt-rich shell of *ca.* 1 nm thick (~ 5 Pt atomic
338 layers, see Supplementary Information S10), and some domains of the hollow structures
339 maintained the Pt-Nd alloy, supporting the *operando* WAXS results.

340

341 In addition to the structure/morphological evolution in the Pt-Nd electrocatalysts, the
342 electrochemical strain dynamics were followed throughout the ADT, see Figure 6a and b. It has
343 been reported that the origin of the electrochemical strain dynamics in NPs comes from the
344 adsorption processes that take place at the electrode/electrolyte interphase,²⁶ whereby the
345 adsorption/desorption events induce NP lattice expansion/contraction at the electrochemical
346 interphase. For the Pt/C benchmark (black profile in Figure 6a and b), in the potential range of
347 $0.05 \leq E \leq 0.30$ V_{RHE}, the hydrogen underpotential deposition (H_{upd}) region (denoted as Pt-H in
348 Figure 6a and b), one can appreciate a reversible lattice expansion, *i.e.*, no hysteresis. In contrast,
349 at $E > 0.5$ V_{RHE}, *i.e.*, the oxygenated species adsorption/desorption region (denoted as Pt-O in
350 Figure 6a and b), the pronounced hysteresis indicates an irreversible structural change due to the

351 Pt oxidation dynamics.³⁹ The results of Figure 6a indicate that, strikingly, the lattice expansion is
352 attenuated in both the Pt-H and Pt-O regions for Pt_{6.1}Nd/C vs. the Pt/C reference, in agreement
353 with a lower H and OH surface coverage, respectively, evoking weaker adsorption energy of both
354 species. This tendency is maintained at the end of the ADT, so confirming by *operando*
355 measurements the benefit of the Pt-Nd alloy. For Pt_{7.8}Nd/C, even though the strain dynamics in
356 the Pt-H region are Pt-like, it seems that there is lower oxide surface coverage, relative to Pt/C,
357 and less intense hysteresis at the Pt-O region is observed. Although the Pt-like behaviour might be
358 explained by the presence of pure Pt architectures, the lower hysteresis (related to the oxide
359 dynamics) in this electrocatalyst could also be linked to an effect on the local morphology,
360 decreasing its local oxophilicity.

361



362
 363 **Figure 6.** Potential-dependency of the relative lattice constant variation of (a) Pt_{6.1}Nd/C and (b)
 364 Pt_{7.8}Nd/C. (c) Electrochemical active surface area (ECSA, determined by CO-stripping), specific
 365 surface activity (I_s), mass activity (I_m) and detected dissolved Pt and Nd in the electrolyte, at the
 366 beginning (BoT) and at the end (EoT) of the 30,00 cycles ADT under nitrogen or oxygen
 367 atmosphere of Pt_{6.1}Nd/C and Pt_{7.8}Nd/C. Pt/C is used as reference.

368
 369 Enhanced kinetics of the sluggish ORR in acidic medium require the binding energies (ΔE) of the
 370 key reaction intermediates, *i.e.*, O* and OH*, to be weaker than with Pt (111) by ~ 0.2 eV and
 371 ~ 0.1 eV, respectively.⁴⁰ The DFT computations performed in this work predict a weaker
 372 adsorption energy change, ΔE_{O^*} and ΔE_{OH^*} , of 0.248 and 0.063 eV *vs.* Pt (111), respectively,
 373 using the Pt₅Nd@5-Pt structure (this model matches better the *operando* experimental results). It

374 may be inferred that the enhanced adsorption properties shown in Figure 6 come from the surface
375 compressive strain rather than the strong Pt-Nd charge transfer, since this electronic perturbation
376 does not go beyond the two first Pt layers. In this work, the DFT results aim at guiding the
377 interpretation of experimental observations rather than strictly predicting the behavior of the
378 complex practical system.

379 The electrochemical activity-stability towards the ORR of the Pt_xNd/C electrocatalysts was
380 evaluated using the RDE technique in 0.1 M HClO₄ electrolyte. The ADT consisted of 30,000
381 square-wave potential cycles between 0.6-0.95 V_{RHE}³⁸ (see the Figure S1 in the Supplementary
382 Information S3). To visualize the possible oxygen adsorption-induced segregation effects, the
383 ADT was carried out in N₂- and O₂-saturated electrolyte, when notable performance differences
384 were observed after 30,000 cycles. The cyclic voltammograms in N₂-saturated 0.1 M HClO₄, at
385 the beginning (BoT) and at the end (EoT) of the ADT of Figure S15 in the Supplementary
386 Information S11 display the features typical of Pt in acidic medium. While the cyclic
387 voltammograms of Pt_{6.1}Nd/C, at BoT and EoT, are characterized by a distorted H_{upd} region due to
388 the modified Pt-H interaction on Pt-REM alloys,¹³ the cyclic voltammograms of Pt_{7.8}Nd/C present
389 an intermediate Pt/Pt-alloy behaviour, in full agreement with the results discussed above.

390

391 As was mentioned above, in terms of specific ORR activity (I_s), the results of Figure 6c confirm
392 that the synthesized Pt-Nd electrocatalysts are intrinsically more active than the Pt/C benchmark,
393 as improvement factors at BoT of 2.7 (Pt_{7.8}Nd/C) and 3.4 (Pt_{6.1}Nd/C) are observed. These features
394 might be directly related to the enhanced adsorption properties shown in Figure 6a and b.
395 Nonetheless, the ORR polarization curves shown in Figure S15 in the Supplementary Information

396 S11 reveal evident degradation after the ADT and highlight a stronger activity loss after the ADT
397 under O₂ atmosphere. This behavior is reflected in the mass-transport-corrected ORR polarization
398 curves (normalized by Pt mass, Figure S16 in the Supplementary Information S11), demonstrating
399 that Pt_{7.8}Nd/C and Pt_{6.1}Nd/C experienced stronger degradation after the ADT under O₂ atmosphere.
400 *Ex situ* ICP-MS measurements of the electrolyte at EoT corroborate these conclusions since higher
401 concentration of dissolved metal was detected after electrochemical cycling in O₂ atmosphere,
402 suggesting higher metal dissolution under these conditions. Although we have shown indirect
403 evidence of the metal dissolution through the ADT, this *ex situ* approach is insufficiently precise,
404 since it is not possible to disentangle the transient dissolution events that take place or quantify the
405 metal dissolution. The ECSA, I_s and I_m values, at the BoT and EoT under both atmospheres, are
406 exposed in Figure 6c and Table 2, with the concentration of dissolved Pt and Nd in the electrolyte.

407

408 **Table 2.** Electrochemical kinetic parameters of Pt_{6.1}Nd/C and Pt_{7.8}Nd/C at BoT and EoT.
409 Commercial Pt/C is used as reference.

	Condition	^a ECSA (m ² g _{Pt} ⁻¹)	I _{s@0.9 V} (mA cm _{Pt} ⁻²)	I _{m@0.9 V} (A mg _{Pt} ⁻¹)	^b Dissolved metal (ng L ⁻¹)
Pt _{7.8} Nd/C	BoT	46.19 ± 2.5	1.19 ± 0.08	0.54 ± 0.04	--
	EoT@N ₂	38.85 ± 2.7	0.79 ± 0.15	0.31 ± 0.08	Pt: 26.4; Nd: 235.4
	EoT@O ₂	36.17 ± 3.5	0.59 ± 0.11	0.21 ± 0.05	Pt: 45.8; Nd: 411.3
Pt _{6.1} Nd/C	BoT	41.00 ± 3.6	1.53 ± 0.07	0.62 ± 0.05	--
	EoT@N ₂	37.01 ± 3.4	1.21 ± 0.08	0.49 ± 0.06	Pt: 18.5; Nd: 127.1
	EoT@O ₂	37.59 ± 3.7	1.02 ± 0.15	0.38 ± 0.05	Pt: 27.6; Nd: 240.6
	BoT	54.41 ± 2.1	0.44 ± 0.07	0.23 ± 0.03	--

Pt/C	EoT@N ₂	45.30 ± 2.7	0.27 ± 0.04	0.12 ± 0.03	Pt: 28.7
	EoT@O ₂	46.02 ± 2.0	0.26 ± 0.03	0.13 ± 0.02	Pt: 32.3

410 a: Determined by CO-stripping; b: Determined by ICP-MS on the electrolyte recovered at EoT.

411

412 From Figure 6c and Table 2 it is concluded that the Pt/C benchmark suffered similar degradation
413 after the ADT under both atmospheres. However, it seems that the degradation of Pt_{7.8}Nd/C and
414 Pt_{6.1}Nd/C is more pronounced after the ADT under O₂ atmosphere. The ECSA variations might be
415 related to the slight particle size changes and morphological transitions provided in the
416 Supplementary Information S11; meanwhile, the activity attenuation of the Pt-Nd electrocatalysts
417 is related to their compositional segregation, and decrease of the kinetic benefit from the alloying
418 effect.

419

420 Theoretical works have suggested that in Pt-based alloys the presence of adsorbed oxygen induces
421 segregation of the non-precious metal to the surface .⁴¹ In fact, due to the larger atomic radii and
422 lower surface energy of REMs relative to Pt, it is expected that the Nd atom tends to segregate to
423 the surface. To obtain insights concerning oxygen-induced segregation of Nd in Pt-Nd alloys, we
424 have performed DFT calculations of the segregation energies (E_{seg}) of the Nd atom on the Pt (111)
425 surface in the presence and absence of oxygen. Figure S20 in the Supplementary Information S12
426 illustrates how the E_{seg} of one Nd atom evolves as a function of its position in the Pt slab in the
427 presence and in the absence of adsorbed oxygen, revealing the strong oxygen-induced segregation
428 of Nd towards the topmost surface layer of Pt (the more negative E_{seg} value, the greater the
429 segregation). The segregation energy of a Nd atom located on the first surface layer interacting
430 with oxygen is more than double that in the absence of oxygen ($E_{\text{seg}} = -4.7$ eV vs. -2.1 eV).

431 Furthermore, the effect of oxygen seems to be limited to the Nd atoms located in the two top layers;
432 the Nd atoms located in the third and fourth layers are found to have a bulk-like behaviour and the
433 presence of oxygen does not induce their segregation. This result is in line with the reported
434 isosurfaces in Pt₅Nd@5-Pt, suggesting the strong segregation of Nd atoms located in the upper
435 surface layers and their dissolution during the ADT under oxygen atmosphere, resulting in Pt-Nd
436 alloy system with constrained Pt outer surface layers.

437

438 **4. CONCLUSION**

439 The Pt_{6.1}Nd composition has the highest ORR activity among the carbon-supported Pt-Nd
440 nanoalloy series. Even though the *ex situ* characterization techniques revealed surface compressive
441 strain and electronic modifications due to the strong charge transfer between Pt and Nd, at the
442 electrochemical operating conditions, the structure of the electrocatalysts underwent significant
443 transformation. The strongest of these were observed during the early electrode conditioning
444 (electrochemical surface activation) rather than through ADT of 5,000 cycles. The *operando*
445 determined electrochemical strain dynamics and DFT predictions provided evidence for enhanced
446 adsorption properties of Pt_{6.1}Nd/C before and after the electrochemical cycling, which are reflected
447 in the ORR activity in the RDE. No significant structural changes were detected during the 5,000
448 cycles ADT under inert (N₂) or reactive (O₂) atmosphere. However, after a 30,000 cycle ADT, the
449 O₂ atmosphere induces higher electrocatalytic activity decay relative to that observed under N₂
450 atmosphere. This behaviour is consistent with Nd segregation induced by oxygen adsorption, and
451 diminished ORR kinetic benefit from the Pt-Nd alloy. Even though the expected high
452 activity/stability on this Pt-REM/C nanoalloys was not observed, the *operando* structure-activity-

453 stability relations described underpin further optimization/understanding of carbon-supported Pt-
454 rare earth nanoalloys as fuel cell cathode catalysts.

455 This study is a contribution to the understanding of the structure-activity-stability relationships of
456 carbon-supported Pt-rare earth nanoalloys under electrochemical conditions.

457

458 **AUTHOR INFORMATION**

459 **Corresponding Author**

460 **Sara Cavaliere*

461 *Email: Sara.Cavaliere@umontpellier.fr*

462

463 **ORCID**

464 C.A. Campos-Roldán: 0000-0002-1517-9037

465 R. Chattot: 0000-0001-6169-530X

466 J.S. Filhol: 0000-0002-3681-9267

467 H. Guesmi : 0000-0002-9369-523X

468 F. Pailloux: 0000-0002-9217-4723

469 P.-Y. Blanchard: 0000-0003-1659-6868

470 A. Zitolo : 0000-0002-2187-6699

471 D. Jones: 0000-0003-3787-2462

472 S. Cavaliere: 0000-0003-0939-108X

473

474 **Author Contributions**

475 The manuscript was written through contributions of all authors. All authors have given approval
476 to the final version of the manuscript.

477 **Author Contributions**

478 **Carlos A. Campos-Roldán** : Writing-original draft, conceptualization, formal analysis,
479 investigation, **Raphaël Chattot** : Writing-review & editing, conceptualization, formal analysis,
480 investigation, **Jean-Sébastien Filhol** : Writing-review & editing, formal analysis, methodology,
481 **Hazar Guesmi** : Writing-review & editing, formal analysis, methodology, **Frédéric Pailloux** :
482 Writing-review & editing, formal analysis, investigation, **Rémi Bacabe** : Investigation, **Pierre-**
483 **Yves Blanchard** : Writing-review & editing, supervision, **Andrea Zitolo** : Writing-review &
484 editing, formal analysis, investigation, **Jakub Drnec** : Writing-review & editing, formal analysis,
485 investigation, **Deborah J. Jones** : Writing-review & editing, conceptualization, funding
486 acquisition, supervision, **Sara Cavaliere** : Writing-review & editing, conceptualization, funding
487 acquisition, supervision

488

489 **ASSOCIATED CONTENT**

490 The following files are available free of charge.

491 **Supporting Information**: Experimental methodology, electrocatalysts optimization and
492 selection, supplementary spectroscopy information, phase stability diagram, characterization
493 after the ADT, and oxygen-induced segregation diagram. are available in the Supporting
494 Information.

495

496 ACKNOWLEDGEMENTS

497 The research leading to these results has received funding from the IMMORTAL project,
498 which receives funding from the Fuel Cells and Hydrogen 2 Joint Undertaking (now Clean
499 Hydrogen Partnership) under grant agreement No 101006641. This Joint Undertaking
500 receives support from the European Union's Horizon 2020 research and innovation
501 programme, Hydrogen Europe and Hydrogen Europe Research. We acknowledge the
502 European Synchrotron Radiation Facility (ESFR) for provision of synchrotron radiation
503 facilities at the ID31 beamline (DOI 10.15151/ESFR-ES-673897258). We also
504 acknowledge Synchrotron SOLEIL (Gif-sur Yvette, France) for provision of synchrotron
505 radiation facilities at beamline SAMBA.

506

507 REFERENCES

- 508 1. van der Spek, M.; Banet, C.; Bauer, C.; Gabrielli, P.; Goldthorpe, W.; Mazzotti, M.;
509 Munkejord, S. T.; Røkke, N. A.; Shah, N.; Sunny, N.; Sutter, D.; Trusler, J. M.; Gazzani, M.,
510 Perspective on the hydrogen economy as a pathway to reach net-zero CO₂ emissions in Europe.
511 *Energy Environ. Sci.* **2022**, *15* (3), 1034-1077.
- 512 2. Cullen, D. A.; Neyerlin, K. C.; Ahluwalia, R. K.; Mukundan, R.; More, K. L.; Borup,
513 R. L.; Weber, A. Z.; Myers, D. J.; Kusoglu, A., New roads and challenges for fuel cells in
514 heavy-duty transportation. *Nat. Energy* **2021**, *6* (5), 462-474.
- 515 3. Kodama, K.; Nagai, T.; Kuwaki, A.; Jinnouchi, R.; Morimoto, Y., Challenges in
516 applying highly active Pt-based nanostructured catalysts for oxygen reduction reactions to fuel
517 cell vehicles. *Nat Nanotechnol* **2021**, *16* (2), 140-147.
- 518 4. Jiao, K.; Xuan, J.; Du, Q.; Bao, Z.; Xie, B.; Wang, B.; Zhao, Y.; Fan, L.; Wang, H.;
519 Hou, Z.; Huo, S.; Brandon, N. P.; Yin, Y.; Guiver, M. D., Designing the next generation of
520 proton-exchange membrane fuel cells. *Nature* **2021**, *595* (7867), 361-369.
- 521 5. Ahn, C. Y.; Park, J. E.; Kim, S.; Kim, O. H.; Hwang, W.; Her, M.; Kang, S. Y.; Park,
522 S.; Kwon, O. J.; Park, H. S.; Cho, Y. H.; Sung, Y. E., Differences in the Electrochemical
523 Performance of Pt-Based Catalysts Used for Polymer Electrolyte Membrane Fuel Cells in Liquid
524 Half- and Full-Cells. *Chem Rev* **2021**, *121* (24), 15075-15140.
- 525 6. Zhao, L.; Zhu, J.; Zheng, Y.; Xiao, M.; Gao, R.; Zhang, Z.; Wen, G.; Dou, H.; Deng,
526 Y. P.; Yu, A.; Wang, Z.; Chen, Z., Materials Engineering toward Durable Electrocatalysts for
527 Proton Exchange Membrane Fuel Cells. *Adv. Energy Mater.* **2021**, *12* (2), 2102665.

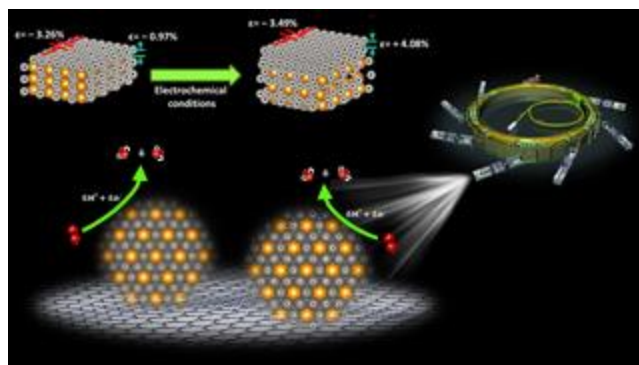
- 528 7. Borup, R. L.; Kusoglu, A.; Neyerlin, K. C.; Mukundan, R.; Ahluwalia, R. K.; Cullen,
529 D. A.; More, K. L.; Weber, A. Z.; Myers, D. J., Recent developments in catalyst-related PEM
530 fuel cell durability. *Curr Opin Electrochem* **2020**, *21*, 192-200.
- 531 8. Greeley, J.; Stephens, I. E.; Bondarenko, A. S.; Johansson, T. P.; Hansen, H. A.;
532 Jaramillo, T. F.; Rossmeisl, J.; Chorkendorff, I.; Norskov, J. K., Alloys of platinum and early
533 transition metals as oxygen reduction electrocatalysts. *Nat Chem* **2009**, *1* (7), 552-6.
- 534 9. Vej-Hansen, U. G.; Rossmeisl, J.; Stephens, I. E.; Schiøtz, J., Correlation between
535 diffusion barriers and alloying energy in binary alloys. *Phys Chem Chem Phys* **2016**, *18* (4),
536 3302-7.
- 537 10. Stephens, I. E. L.; Bondarenko, A. S.; Bech, L.; Chorkendorff, I., Oxygen
538 Electroreduction Activity and X-Ray Photoelectron Spectroscopy of Platinum and Early
539 Transition Metal Alloys. *ChemCatChem* **2012**, *4* (3), 341-349.
- 540 11. Escudero-Escribano, M.; Verdaguer-Casadevall, A.; Malacrida, P.; Gronbjerg, U.;
541 Knudsen, B. P.; Jepsen, A. K.; Rossmeisl, J.; Stephens, I. E.; Chorkendorff, I., Pt₅Gd as a
542 highly active and stable catalyst for oxygen electroreduction. *J Am Chem Soc* **2012**, *134* (40),
543 16476-9.
- 544 12. Malacrida, P.; Escudero-Escribano, M.; Verdaguer-Casadevall, A.; Stephens, I. E. L.;
545 Chorkendorff, I., Enhanced activity and stability of Pt–La and Pt–Ce alloys for oxygen
546 electroreduction: the elucidation of the active surface phase. *J. Mater. Chem. A* **2014**, *2* (12),
547 4234-4243.
- 548 13. Escudero-Escribano, M.; Malacrida, P.; Hansen, M.; Vej-Hansen, U.; Velázquez-
549 Palenzuela, A.; Tripkovic, V.; Schiøtz, J.; Rossmeisl, J.; Stephens, I.; Chorkendorff, I., Tuning
550 the activity of Pt alloy electrocatalysts by means of the lanthanide contraction. *Science* **2016**, *352*
551 (6281), 73-76.
- 552 14. Hernandez-Fernandez, P.; Masini, F.; McCarthy, D. N.; Strebel, C. E.; Friebel, D.;
553 Deiana, D.; Malacrida, P.; Nierhoff, A.; Bodin, A.; Wise, A. M.; Nielsen, J. H.; Hansen, T.
554 W.; Nilsson, A.; Stephens, I. E.; Chorkendorff, I., Mass-selected nanoparticles of Pt_xY as model
555 catalysts for oxygen electroreduction. *Nat Chem* **2014**, *6* (8), 732-8.
- 556 15. Velázquez-Palenzuela, A.; Masini, F.; Pedersen, A. F.; Escudero-Escribano, M.;
557 Deiana, D.; Malacrida, P.; Hansen, T. W.; Friebel, D.; Nilsson, A.; Stephens, I. E. L.;
558 Chorkendorff, I., The enhanced activity of mass-selected Pt_xGd nanoparticles for oxygen
559 electroreduction. *J. Catal.* **2015**, *328*, 297-307.
- 560 16. Pedersen, A. F.; Ulrikkeholm, E. T.; Escudero-Escribano, M.; Johansson, T. P.;
561 Malacrida, P.; Pedersen, C. M.; Hansen, M. H.; Jensen, K. D.; Rossmeisl, J.; Friebel, D.;
562 Nilsson, A.; Chorkendorff, I.; Stephens, I. E. L., Probing the nanoscale structure of the
563 catalytically active overlayer on Pt alloys with rare earths. *Nano Energy* **2016**, *29*, 249-260.
- 564 17. Hu, Y.; Jensen, J. O.; Norby, P.; Cleemann, L. N.; Yang, F.; Li, Q., Mechanistic
565 Insights into the Synthesis of Platinum–Rare Earth Metal Nanoalloys by a Solid-State Chemical
566 Route. *Chem. Mater.* **2021**, *33* (2), 535-546.
- 567 18. Hu, Y.; Jensen, J. O.; Cleemann, L. N.; Brandes, B. A.; Li, Q., Synthesis of Pt-Rare
568 Earth Metal Nanoalloys. *J Am Chem Soc* **2020**, *142* (2), 953-961.
- 569 19. Kanady, J. S.; Leidinger, P.; Haas, A.; Titlbach, S.; Schunk, S.; Schierle-Arndt, K.;
570 Crumlin, E. J.; Wu, C. H.; Alivisatos, A. P., Synthesis of Pt₃Y and Other Early-Late
571 Intermetallic Nanoparticles by Way of a Molten Reducing Agent. *J Am Chem Soc* **2017**, *139*
572 (16), 5672-5675.

- 573 20. Itahara, H.; Takatani, Y.; Takahashi, N.; Kosaka, S.; Nagoya, A.; Inaba, M.;
574 Kamitaka, Y.; Morimoto, Y., Synthesis of Carbon-Supported Intermetallic Pt₅Ce Compound
575 Nanoparticles via a Water-Based Impregnation Route. *Chem. Mater.* **2021**, *34* (1), 422-429.
- 576 21. Gunji, T.; Tanaka, S.; Inagawa, T.; Otsuka, K.; Matsumoto, F., Atomically Ordered
577 Pt₅La Nanoparticles as Electrocatalysts for the Oxygen Reduction Reaction. *ACS Appl. Nano*
578 *Mater.* **2022**, *5* (4), 4958-4965.
- 579 22. Campos-Roldán, C. A.; Jones, D. J.; Rozière, J.; Cavaliere, S., Platinum-Rare Earth
580 Alloy Electrocatalysts for the Oxygen Reduction Reaction: A Brief Overview. *ChemCatChem*
581 **2022**, *14* (19), e202200334.
- 582 23. Campos-Roldán, C. A.; Parnière, A.; Donzel, N.; Pailloux, F.; Blanchard, P.-Y.;
583 Jones, D. J.; Rozière, J.; Cavaliere, S., Influence of the Carbon Support on the Properties of
584 Platinum–Yttrium Nanoalloys for the Oxygen Reduction Reaction. *ACS Applied Energy*
585 *Materials* **2022**, *5* (3), 3319-3328.
- 586 24. Timoshenko, J.; Roldan Cuenya, B., In Situ/Operando Electrocatalyst Characterization by
587 X-ray Absorption Spectroscopy. *Chem Rev* **2021**, *121* (2), 882-961.
- 588 25. Sasaki, K.; Marinkovic, N.; Isaacs, H. S.; Adzic, R. R., Synchrotron-Based In Situ
589 Characterization of Carbon-Supported Platinum and Platinum Monolayer Electrocatalysts. *ACS*
590 *Catal.* **2015**, *6* (1), 69-76.
- 591 26. Chattot, R.; Martens, I.; Mirolo, M.; Ronovsky, M.; Russello, F.; Isern, H.; Braesch,
592 G.; Hornberger, E.; Strasser, P.; Sibert, E.; Chatenet, M.; Honkimaki, V.; Drnec, J.,
593 Electrochemical Strain Dynamics in Noble Metal Nanocatalysts. *J Am Chem Soc* **2021**, *143* (41),
594 17068-17078.
- 595 27. Kawaguchi, T.; Komanicky, V.; Latyshev, V.; Cha, W.; Maxey, E. R.; Harder, R.;
596 Ichitsubo, T.; You, H., Electrochemically Induced Strain Evolution in Pt-Ni Alloy Nanoparticles
597 Observed by Bragg Coherent Diffraction Imaging. *Nano Lett* **2021**, *21* (14), 5945-5951.
- 598 28. Fuchs, T., Drnec, J., Calle-Vallejo, F., Stubb, N., Sandbeck, D., Ruge, M., Cherevko, S.,
599 Harrington, D., Magnussen, O., Structure dependency of the atomic-scale mechanisms of
600 platinum electro-oxidation and dissolution. *Nat Catal* **2020**, *3*, 754-761.
- 601 29. Campos-Roldán, C. A.; Pailloux, F.; Blanchard, P.-Y.; Jones, D. J.; Rozière, J.;
602 Cavaliere, S., Rational Design of Carbon-Supported Platinum–Gadolinium Nanoalloys for
603 Oxygen Reduction Reaction. *ACS Catal.* **2021**, *11* (21), 13519-13529.
- 604 30. Campos-Roldan, C. A.; Pailloux, F.; Blanchard, P. Y.; Jones, D. J.; Roziere, J.;
605 Cavaliere, S., Enhancing the activity and stability of carbon-supported platinum-gadolinium
606 nanoalloys towards the oxygen reduction reaction. *Nanoscale Adv* **2021**, *4* (1), 26-29.
- 607 31. Gan, L.; Heggen, M.; O'Malley, R.; Theobald, B.; Strasser, P., Understanding and
608 controlling nanoporosity formation for improving the stability of bimetallic fuel cell catalysis.
609 *Nano Lett* **2013**, *13* (3), 1131-8.
- 610 32. Guo, Q.; Kleppa, O., Standard Enthalpies of Formation of Neodymium Alloys, Nd + Me
611 (Me = Ni, Ru, Rh, Pd, Ir, Pt), by High-Temperature Direct Synthesis Calorimetry. *Metall. Mater.*
612 *Trans. B* **1995**, *26B*, 275-279.
- 613 33. Liu, J.; Tennessen, E.; Miao, J.; Huang, Y.; Rondinelli, J.; Heinz, H., Understanding
614 Chemical Bonding in Alloys and the Representation in Atomistic Simulations. *J. Phys. Chem. C*
615 **2018**, *122*, 14996–15009.
- 616 34. Luo, M.; Guo, S., Strain-controlled electrocatalysis on multimetallic nanomaterials. *Nat.*
617 *Rev. Mater.* **2017**, *2* (11), 17059.

- 618 35. Filhol, J. S.; Simon, D.; Sautet, P., Stress induced nanostructure in a Pd monolayer on
619 Ni(110): a first principles theoretical study. *Surf. Sci.* **2001**, *472* (1), L139-L144.
- 620 36. Filhol, J. S.; Simon, D.; Sautet, P., Understanding the High Activity of a Nanostructured
621 Catalyst Obtained by a Deposit of Pd on Ni: First Principle Calculations. *J. Am. Chem. Soc.*
622 **2004**, *126* (10), 3228-3233.
- 623 37. Filhol, J. S.; Saint-Lager, M. C.; De Santis, M.; Dolle, P.; Simon, D.; Baudoing-
624 Savoie, R.; Bertolini, J. C.; Sautet, P., Highly Strained Structure of a Four-Layer Deposit of Pd
625 on Ni(110): A Coupled Theoretical and Experimental Study. *Phys. Rev. Lett.* **2002**, *89* (14),
626 146106.
- 627 38. Stariha, S.; Macauley, N.; Sneed, B. T.; Langlois, D.; More, K. L.; Mukundan, R.;
628 Borup, R. L., Recent Advances in Catalyst Accelerated Stress Tests for Polymer Electrolyte
629 Membrane Fuel Cells. *J. Electrochem. Soc.* **2018**, *165* (7), F492-F501.
- 630 39. Martens, I.; Chattot, R.; Rasola, M.; Blanco, M. V.; Honkimäki, V.; Bizzotto, D.;
631 Wilkinson, D. P.; Drnec, J., Probing the Dynamics of Platinum Surface Oxides in Fuel Cell
632 Catalyst Layers Using in Situ X-ray Diffraction. *ACS Appl. Energy Mater.* **2019**, *2* (11), 7772-
633 7780.
- 634 40. Čolić, V.; Bandarenka, A. S., Pt Alloy Electrocatalysts for the Oxygen Reduction
635 Reaction: From Model Surfaces to Nanostructured Systems. *ACS Catal.* **2016**, *6* (8), 5378-5385.
- 636 41. Sarwar, M.; Gavartin, J. L.; Martinez Bonastre, A.; Garcia Lopez, S.; Thompsett, D.;
637 Ball, S. C.; Krzystala, A.; Goldbeck, G.; French, S. A., Exploring fuel cell cathode materials
638 using ab initio high throughput calculations and validation using carbon supported Pt alloy
639 catalysts. *Phys Chem Chem Phys* **2020**, *22* (10), 5902-5914.

640

641 **TOC graphic**



642

643

644